JOURNAL OF GEOPHYSICAL RESEARCH, VOL. 97, NO.C4, PAGES 5651-5664, APRIL 15, 1992

Observed Growth of Langmuir Circulation

JEROME A. SMITH

Scripps Institution of Oceanography, University of California at San Diego, La Jolla, California

Surface velocity patterns and upper ocean density profiles are presented from a period following a sudden increase in wind. A prior wind speed of 8 m/s failed to produce visible signs of Langmuir circulation. After the wind speed increased to 13 m/s, Langmuir circulation developed within 15 min. The initial scale observed was about 16 m, streak to streak, and may have been restricted by the depth scale of the measurements. This spacing is about two thirds of the dominant wavelength (4-s-period waves). The streak spacing (two cell widths) increased at roughly 40 m/h for the next hour. The density measurements indicate a depth of mixing which increased over the same period at a rate of 20 m/h; thus the vertical to horizontal aspect ratio was about 1:1. Prior stratification was weak (buoyancy frequency of about 1.5 cph), and probably did not affect the circulation initially.

1. INTRODUCTION

Mixing at the surface of the oceans is important to a wide variety of concerns, including global climate and the health of marine life. Two main causes of this mixing can be identified: (1) when surface water is cooled, it becomes denser and sinks, mixing downward either to the bottom or until limited by the pre-existing stratification; and (2) the wind can mechanically stir the surface layer to some depth, usually limited by stratification. The former can result in mixing to considerable depths, but the latter occurs more often, over the majority of the world oceans. Frequently, the two driving forces occur together. What are the details of this mixing? For example, are bubbles dragged deep into the mixed layer, injecting gases at depth? Are there repeatable features which could lead to improved models of surface mixing and its effects?

When wind blows over water, lines are often visible on the surface, running roughly parallel to the wind. In an exemplary series of experiments, *Langmuir* [1938] found these to be lines of convergence along the surface, with downwelling below each line. He found also that maxima in the downwind surface currents occur along these lines. Thus the mixing layer is organized into rolls of alternating sign, aligned with the wind, and water parcels follow helical paths downwind. This form of circulation in surface layers of water has come to be called "Langmuir circulation." Historically, this term has not implied any particular mechanism of formation, and it generally has not been used in reference to other similar structures (e.g., roll vortices in the atmosphere or in wall-bounded convection). Langmuir [1938, p. 123] expressed his belief that "the helical vortices set up by wind apparently constitute the essential mechanism by which the epilimnion is produced." Clearly, this form of "helical vortices" is efficient in transporting momentum, energy, and matter throughout the surface layer of water.

Three mechanisms are currently considered to drive Langmuir circulation. (1) An interaction between surface waves and wind-driven shear gives rise to this form of circulation as a linear instability. A review of this theory, and of observations before 1983, is given by *Leibovich* [1983]. (2) Even without surface waves, turbulent mixing will occur due to the breakdown of the wind-induced surface shear layer. Much of what is known in this case is derived from laboratory experiments [e.g., *Rohr and Van Atta*, 1987]. (3) Circulation of similar form can also arise as an instability of an Ekman layer [e.g., *Leibovich and Lele*, 1985]. The last may influence later development, but Langmuir circulation is often observed to form within minutes after the onset of wind, long before rotational effects should be important. Does the wave interaction provide an effective way to tap the enormous energy available from surface waves?

Observations to date have focused mainly on "quasi-steady" Langmuir circulation, where the scale of the circulation is evolving slowly if at all [e.g., *Weller et al.*, 1985; *Smith et al.*, 1987; *Pollard and Thomas*, 1989]. These have provided only glimpses into the overall structure and evolution of the flow. Many questions remain. How quickly does mixing occurs after the onset of wind? How quickly is a quasi-steady state achieved? Do all scales of circulation grow simultaneously, with the larger scales of circulation appearing later owing to slower growth rates? Or is there evolution to larger scales, in which the smaller scales give up energy to the larger scales as the evolution proceeds?

Here, observations are presented from a time period including a sudden increase in wind, followed by rapid evolution of Langmuir circulation from small to larger scale. Velocities were monitored simultaneously along subsurface transects in several directions, using Doppler sonar technology. This allows the scales and amplitude of circulation to be tracked as a function of time. The observed evolution follows the latter of the aforementioned possibilities: velocity variance associated with one briefly dominant scale decreases when the circulation evolves to larger scales. The total variance of the cross-wind component of surface velocity roughly tracks the wind stress (with some time averaging), without regard to the scale of the underlying flow. The evolution from initially small scales to a "quasi-steady state" occurred within a time span of less than an hour.

2. EXPERIMENTAL SETUP

2.1 *Setting*

An extensive set of observations was made as part of the "Surface Wave Process Program" (SWAPP). The experiment took place at 35°N, 127°W, roughly 500 km off the coast of California (see Figure 1). The research platform *FLIP* was on location (moored) from February 24, 1990 through March 18, 1990. The Canadian vessel CSS *Parizeau*, the US Navy tugboat

Paper number 91JC03118.
0148-0227/92/91JC=03118$05.00

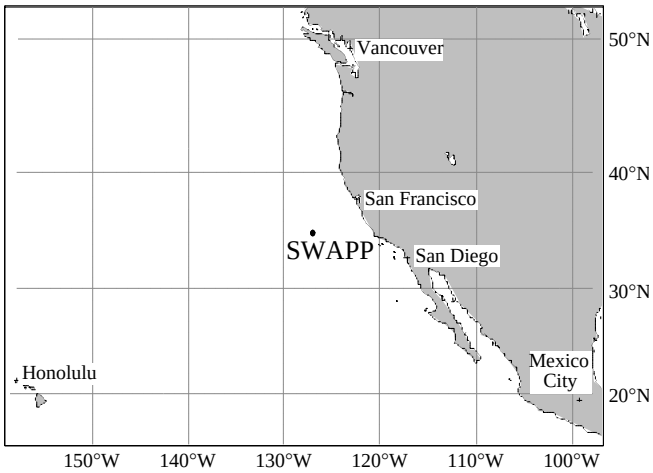

Fig. 1. Location of SWAPP site. SWAPP took place in February and March 1990, at 35°N, 127°W, about 500 km off the coast of California. The ocean bottom at the site is flat, and the depth is roughly 4000 m.

Navajo, and the R/V *DeSteiguer* were also involved in coordinated scientific studies. The focus here is on data from a new high-resolution sonar system, together with nearly continual measurements of the upper-ocean density profile made with a rapidly profiling Conductivity, Temperature and Depth system (CTD), both deployed on R/P *FLIP*. We also have data from a long range sonar system, and observations made by other participants include two- and three-component winds, two- and three-component currents throughout the depth of the mixed layer, ambient noise characteristics, vertical structure of bubble plumes, turbulence levels, and sea floor microseism activity (see *Weller et al.* [1991] for a complete list). The richness of this combined data set should facilitate future efforts to relate observed aspects of Langmuir circulation to atmospheric forcing and preexisting stratification.

The time period described here began on March 4, 1990, when there was a sudden onset of wind from the northwest (Figure 2). Several other strong wind events were encountered, but this one had a dramatic start: the wind stress nearly tripled in less than a minute (the wind rose from 8 m/s at 0720 to 13 m/s at 0721, PST). A swell peak in the surface wave field preceded the wind. At the onset of the strong winds, the dominant wind and wave directions differed by about 25°. The wind dipped below 10 m/s between 0830 and 0930, then returned to 13 m/s by about 1030. It then blew fairly steadily until about 0900 on March 5, after which it dropped rapidly. Over the first part of the wind event (from 0500 through 1130 March 4), the skies were overcast, with mist and occasional light rain. Here, the main focus is on the 3 hours surrounding the onset of strong winds, from 0700 to 1000, March 4. At 0630, just before the increase in wind, the air temperature was 13.28°C, and the sea surface temperature was 12.9°C. At 0930 the air was 12.95°C, and the SST was 12.62°C. Thus the air-sea temperature difference slightly favored stable conditions during this time.

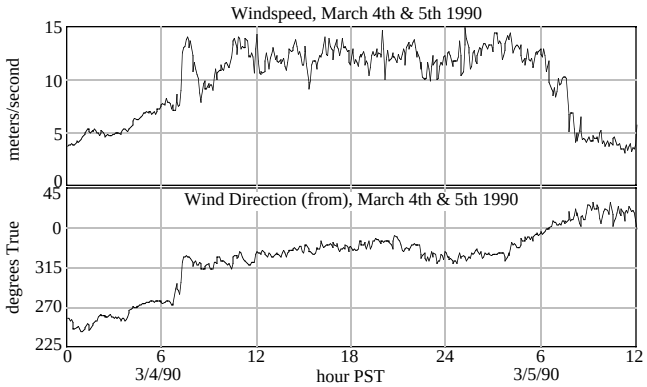

Fig. 2. Wind speed and direction, March 4-5, 1990. On March 4, the wind increased gradually from 3 to 8 m/s between midnight and 0700 PST. Then it jumped suddenly to about 13 m/s at 0721, coincident with a 45° shift in direction. (Wind data provided by A. Plueddemann, Woods Hole Oceanographic Institution.) Focus here is on the 3-hour segment surrounding this jump in windspeed, from 0700 to 1000 PST.

2.2 *Doppler Sonar Configuration*

Four Doppler sonar systems were deployed on the R/P *FLIP* for the duration of SWAPP. Of these, two were designed and operated to monitor surface velocities [c.f. *Smith*, 1989], in order to track both surface wave directional spectra and the lower frequency motions described here (Figure 3). One, operated at 195 kHz, had better range resolution (3 m) but less total range (~400 m). The other, operated at 67 and 80 kHz, achieved ranges of 1 km (limited by timing considerations), with 12 m resolution. The high-resolution (HR) system consisted of 4 beams at 45° increments, and the long-range (LR) system had six beams (see Figure 3). The two systems together cover almost 3 orders of magnitude in scale, from 3 m to 2 km. The initial growth

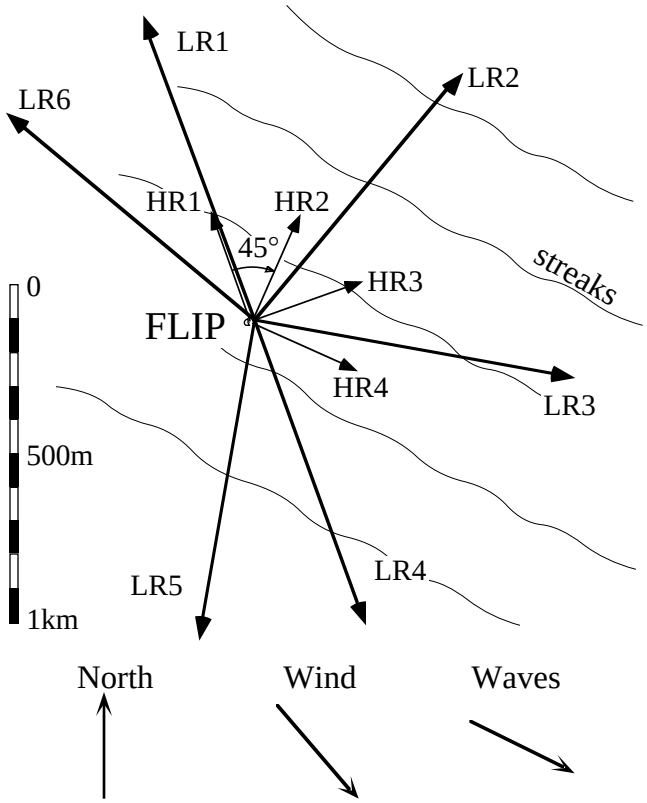

Fig. 3. Plan view of the 10 surface-scanning Doppler sonar beams, roughly to scale. The orientation of *FLIP*, wind, and waves are for the period just after the sudden onset of wind (0730 PST March 4, 1990). Also, the approximate orientation of the surface convergence lines is schematically shown (but with much wider spacing than observed). The focus here is on the "high resolution" (HR) system, which reached to 400 m from *FLIP* with velocity estimates every 3 m. The long range (LR) system reached to 1000 m with 12 m resolution.

described here is relatively small scale, so the HR sonar data provide the focus of this paper.

The surface-scanning Doppler sonars have beam patterns which are narrow azimuthally, but broad in the vertical (about 2/3° by 22° beam widths for the HR sonar). The echoes at these frequencies are dominated by backscatter from bubbles. At 195 kHz the resonant bubble size is about 15 μm, and at 75 kHz it is near 40 μm. The vertical extent of the measurement volume is confined by the form of the near-surface bubble layer and bubble clouds (Figure 4). The intensity of the backscatter from bubbles can vary by a factor of 1000, but the bubbles are believed to remain strongly surface trapped, both inside and outside the denser bubble clouds, with a profile roughly equivalent to exponential decay having a depth scale of about 1 to 1.5 m [*Thorpe,* 1986; *Crawford and Farmer,* 1987]. This "bubble layer" is continuous in winds over 3 to 4 m/s, and dominates the backscatter signal. The same depth scale applies to the vertical weighting of the sonar measurements; thus the vertical extent of the measurements is about 2 to 3 m, from the surface downward. The extent of the measurement volume in range is determined by the duration of transmitted pulse and the amount of range averaging (both corresponding to 3 m for the HR system), while the azimuthal dimension is set by the narrow azimuthal beam width (e.g., at 250 m, 2/3° corresponds to about 3 m). Thus this beam geometry minimizes sensitivity to pitch and roll of the platform, while maintaining measurement volumes of about (3 m)^3 just below the ocean surface, and following (to the extent allowed by geometry) the vertical excursions of the fluid (a water-bubble mixture) there. The resulting measurements are "semi-Lagrangian," following fluid parcels in the vertical but not in the horizontal directions.

Velocity estimates were formed by the standard complex autocovariance technique, as modified for incoherent, repeat-sequence coded sonars [*Rummler,* 1968; *Pinkel,* 1981;*Pinkel and Smith,* 1991]. The HR sonars transmitted a 4-bit "repeat-sequence code" [*Pinkel and Smith,* 1991] every 3/4 s. Covariance estimates were averaged in range for 4 ms (3 m), yielding an estimated rms error of about 10 cm/s in each range bin per transmission (ping). Recording every ping allows the surface wave directional spectrum to be estimated. The swell peak and wind-wave evolution referred to here are derived from a "quick look" surface wave analysis of the HR sonar data (see below). To examine the underlying lower frequency motions, 1-min averages of the velocity data were formed. For the HR system, this corresponds to 80 pings, reducing the rms velocity error to about 1 cm/s. For most of the experiment, data collection alternated hourly between "wave mode" runs, in which every ping is recorded (~52 min duration), and "LC mode" runs, recording just 1-min averages (~68 min). During the initial 8 hours of the March 4 wind event (from roughly 0800 to 1600 PST), "wave mode" data were collected continuously to facilitate study of wave growth and wave-current interactions.

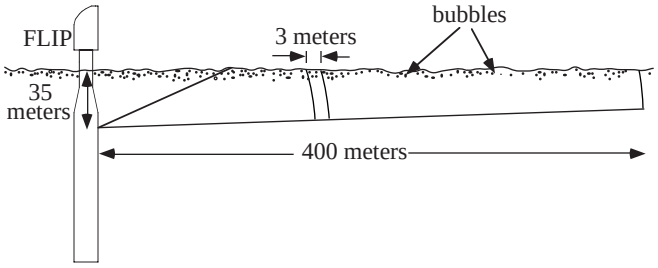

Fig. 4. Schematic view of a sonar beam intersecting the near surface bubble cloud. The bubbles decrease in number with depth, with roughly an exponential profile. The depth scale of the decay is about 1 to 1.5 m. Acoustic backscatter from the bubble cloud completely dominates the return.

2.3 *Surface Wave Analysis*

A "quick look" wave analysis was implemented to obtain quick, robust estimates of the wave directional-frequency spectra. This was used, for example, in estimating the dominant wave direction shown in Figure 3. HR sonar velocity estimates from 108 to 300 m along each beam (64 estimates) were used. A frequency Fast Fourier Transform (FFT) was performed on 4096 samples in time (about 51 min) at each range. For each frequency, a spatial FFT was performed, and the results squared to provide velocity variance-density estimates on a grid of frequency versus along-beam wavenumber, $P(f, k_r)$, where $0 \le f < 1$ Hz and $(-1/6) \le k_r \le (1/6)$ cycles/m (cpm). These were averaged over 32-point frequency bands, yielding an effective frequency resolution of (1/96) Hz. For each value of f and k_r, the linear dispersion relation yields a corresponding angle θ between the sonar beam and the direction of propagation of a surface wave. Since only the range component of velocity is measured, the velocity variance densities are effectively preweighted by $\cos^2\theta$. For angles nearing 90°, the along-beam component vanishes, leaving only noise. Over all points where this angle is real, the density estimates were weighted by an additional $\cos^2\theta$, and the results summed separately over positive and negative values of k_r. This reduces the effects of noise and also suppresses harmonics present in the actual waveforms. Each HR beam thus provides two oppositely directed estimates at each frequency. The results are eight directional estimates at each frequency, each with a net angular weighting of $\cos^4\theta$, spaced at 45° increments around *FLIP*'s average heading over the run. These were scaled according to the linear gravity wave dispersion relation to be equivalent to frequency-weighted spectral densities of (total) slope (i.e., dimensionless spectra). This approach produces estimates with a directional spread of not less than 45°, but there is no known bias in the mean direction computed from the result. The reliability of the mean direction estimate is most likely limited by the statistical variability of the waves over a finite sample interval. The 52-min averages shown here should be reliable to within a few degrees.

Besides being quick, this technique reduces the need to correct for changes in the heading of *FLIP* at each ping. Over a typical time interval used for directional wave estimation (selected to avoid major heading changes), the heading of *FLIP* varied by about 3° rms. At 300 m range, a 3° heading change corresponds to about 16 m in the cross-beam direction. A 16 m wavelength corresponds to 3.2-s-period surface waves, so this must clearly be accounted for in the analysis of the higher-frequency waves. The quick-look analysis limits the angular window of each beam to waves propagating within ±22.5° of parallel to the beam. At 22.5° off the beam direction, a cycle in 16 m perpendicular to the beam corresponds to a wavelength of 6 m, or a frequency of about 2 s. Also, the technique reduces sensitivity to phase variability by summing magnitudes, so that effects of the angular variations are limited mainly to smoothing the variance in both direction and frequency. Since the heading variability affects the results in a way that depends on the frequency (wavenumber) of the waves, caution should be exercised in interpreting, for example, spectral slope with frequency, especially over periods less than 3 s. The variations in azimuth can be accounted for by incorporating the

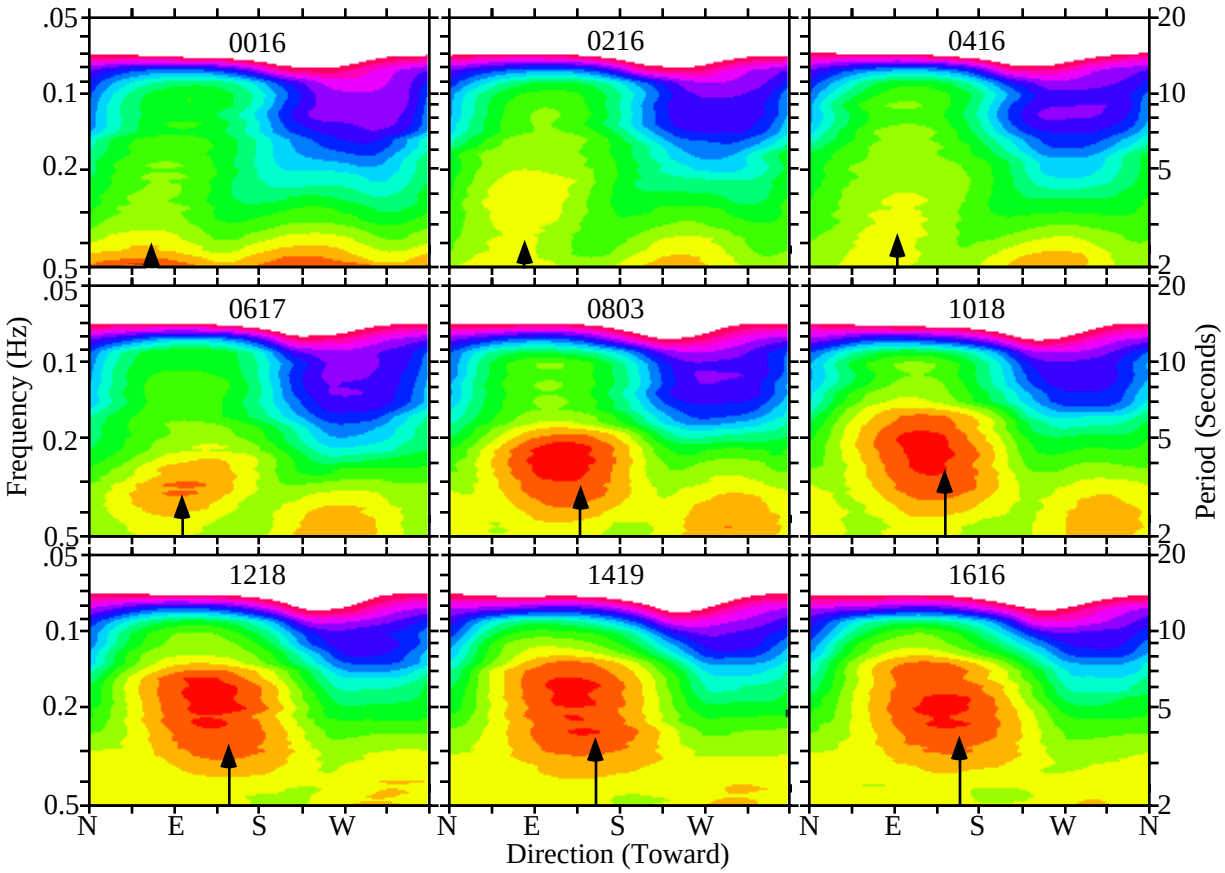

Plate 1. Directional wave spectra, from the "quick-look" analysis of the HR sonar data. The dimensionless spectral density is contoured, with a 2 dB contour interval: $(2\pi/g)^2 f^3 |\hat{V}|^2(f)$, where f is in Hertz and $|\hat{V}|^2(f)$ is the spectral density of the total surface orbital velocity variance per Hertz per cycle. The maximum contour level is -7 dB; the circular integral (over direction) leads to a maximum "saturation level" of 0.003. The wind is indicated by a black arrow at the direction toward which the wind is blowing, with length proportional to the windspeed averaged over the same data segment. A swell peak rises near 10-s periods between midnight and 0400. Higher frequency "seas" appear first in the "0617" spectrum, when the wind was up to 8 m/s. Note that the higher-frequency waves "track" the wind direction quickly, while the lower-frequency waves take longer to adjust.

recorded heading at each moment. A simple FFT in time cannot be performed first, so most currently popular estimation techniques are inapplicable. However, the directional resolution commensurate with the 400-m aperture of the array (2 km including the LR sonar) makes the effort worthwhile. Work on this is underway. These quick-look results are mainly intended to show dominant frequencies and directions, to help with interpretation of lower frequency motions such as described here.

2.4 *CTD Operation*

Density measurements were obtained with a rapidly-profiling CTD system. This consisted of two Seabird CTDs which were modified to operate at 4 m/s drop rate, and which included both regular and high-resolution conductivity sensors. The CTDs were raised and lowered automatically at 4 m/s, completing a down-and-up cycle every 130 s. The two CTDs were deployed over two overlapping depth ranges, from 5 to 220 m and from 200 to 420 m, in an effort to capture Nyquist frequency activity throughout the seasonal thermocline. The resolution in depth (with the regular conductivity sensor) is about 1 m.

3. DATA

3.1 *Waves*

Directional spectra were computed every 2 hours through the wind event. For display, these are rotated according to the average heading of *FLIP* over the 52-min interval, and interpolated to a 5° grid using the $\cos^4\theta$ basis functions. A selection of directional spectra over the initial period of the wind event is shown in Plate 1. A swell peak arose between about 2200 PST on March 3 and 0200 on March 4, about 6 h prior to the onset of strong winds.

3.2 *Surface Currents*

The HR sonar velocity data show the evolution of the surface flow field after the onset of strong winds. At this onset, the wind direction changed by about 45°. Although the mooring constrained *FLIP*'s rotation, *FLIP* was able to rotate roughly with the wind over this particular period (Figure 5). The cross-wind direction remained between HR beams 2 and 3. The cross-wave direction after the change was approximately along HR beam 2 (see Figure 3). The wave direction was estimated from data over the time interval from 0803 to 0854 (Plate 1, center). Over the few hours after the sudden change, both the wind and *FLIP* varied in heading by about 15°, with relative extremes occuring at about 0730 and 0830, and with *FLIP* essentially tracking the wind direction (Figure 5).

Plate 2 shows contours of velocity from 90 to 390 m in range along each of the four HR beams, over the time period from 0700 to 1000 PST March 4, 1990. The velocities shown are averages over 1 min, with 3 m range resolution as described above. A range mean was removed from each profile (beam) prior to

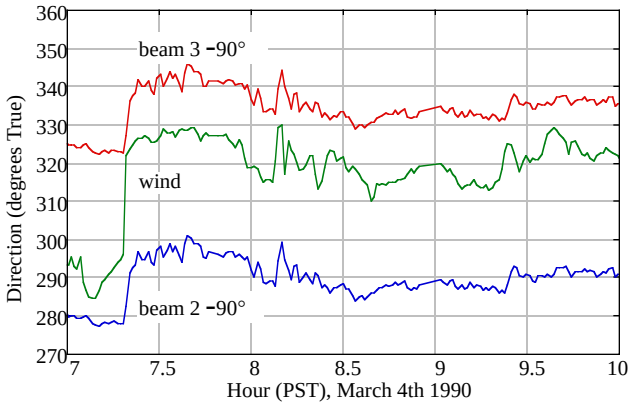

Fig. 5. Directions of the wind and HR sonar beams 2 and 3, over the time period 0700 to 1000, March 4, 1990. The cross-wind direction remained between beams 2 and 3 throughout the wind event. *FLIP*'s orientation closely tracked the variations in wind direction over the 3 hours shown here.

display. Plate 2 is uncorrected for geometric distortion due to the depth of the instrument (35 m): the "range" displayed is range from the instrument, not along the surface. From 90 to 390 m, this geometric distortion is small: 90 m slant range corresponds to 83 m along the surface, and 390 m corresponds to 388 m.

To aid in understanding Plate 2, it is useful to discuss briefly what patterns should result from the mean flow past *FLIP*. For uniform flow advecting stationary, regularly spaced features past the sonars, the time variations would be similar at all ranges along all four beams. For elongated features, "stripes" would appear on the time-range maps of velocity. These would vary in apparent slope, depending on the relative angles of the beam, mean flow, and major axes of the features. For example, looking at Figure 3, imagine that the "streaks" move uniformly southward across the sonar beams.

The means removed from each beam are shown in Figure 6. These were formed over the 1 min by 300 m aperture of each beam. No attempt was made to combine redundant information into improved estimates of the means: the four beams were treated independently. The beginning of an inertial current is apparent in Figure 6: the mean flow is away from *FLIP* along HR4 at 0740 am, but rotates toward the direction approaching *FLIP* along HR2 over the next few hours. The effect of a mean flow combined with variations in *FLIP*'s heading appears only in the range means (not in Plate 2). For example, note the jumps at 0720 and spikes at 0810 in Figures 5 and 6. These means are not corrected for the motion of *FLIP* within its mooring constraints (a few hundred m watch circle); however, *FLIP*s motion is available

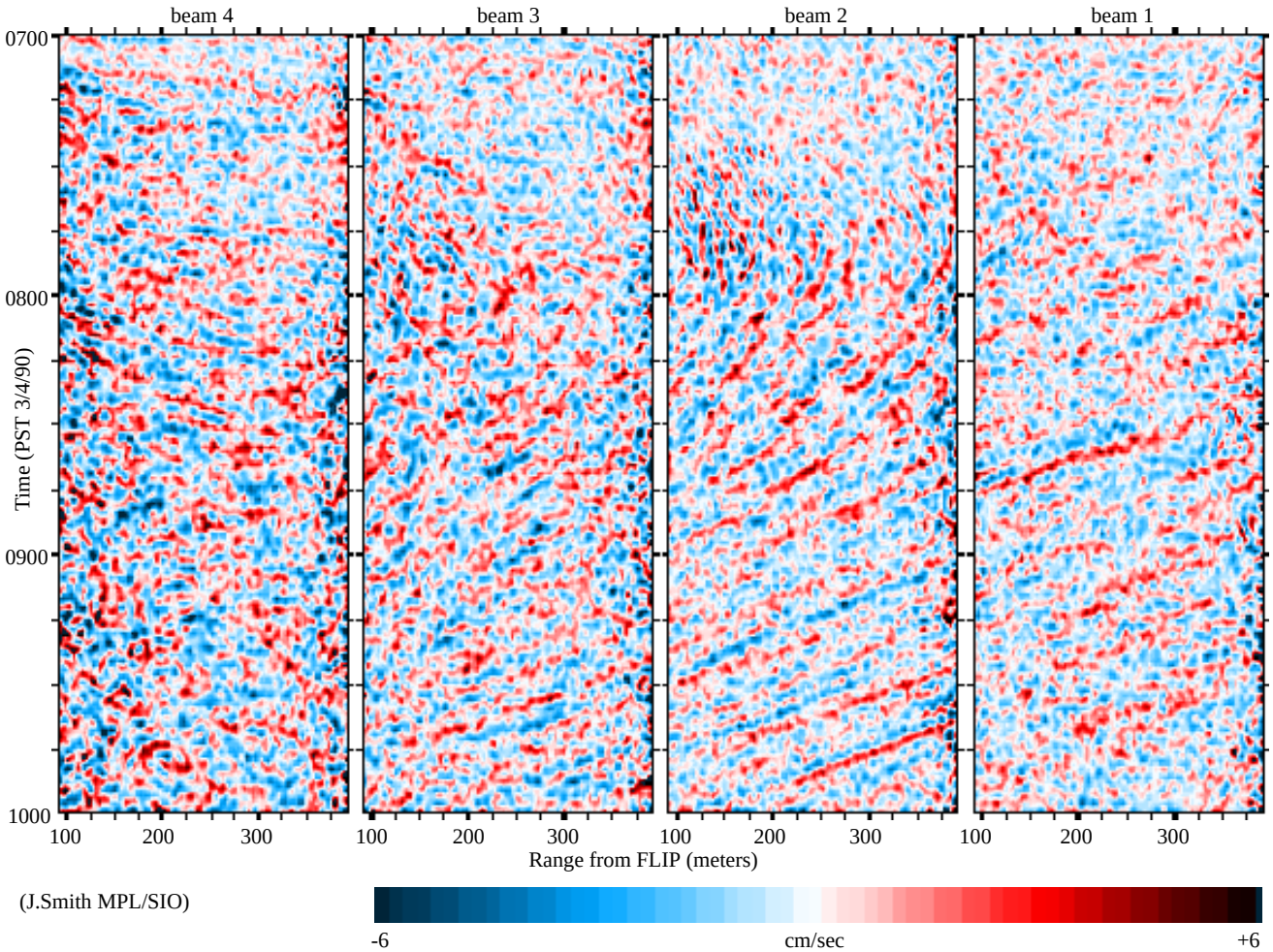

Plate 2. Range-component of velocity versus time and distance, for each of the four HR beams. For display, the data have been low-pass filtered with half-power points at a period of about 3 min and wavelength of 9 m. The mean velocities along each beam have been removed. The "streaks" appearing at various angles arise from the advection of nearly stationary features past *FLIP* by the mean flow. In particular, note that the ripples in beam 2 are stable in range before 0800, and then "accelerate" toward *FLIP*. This reflects the acceleration of the observed mean flow. Note also that the ripples are initially finely spaced (especially at 0730), then the spacing increases.

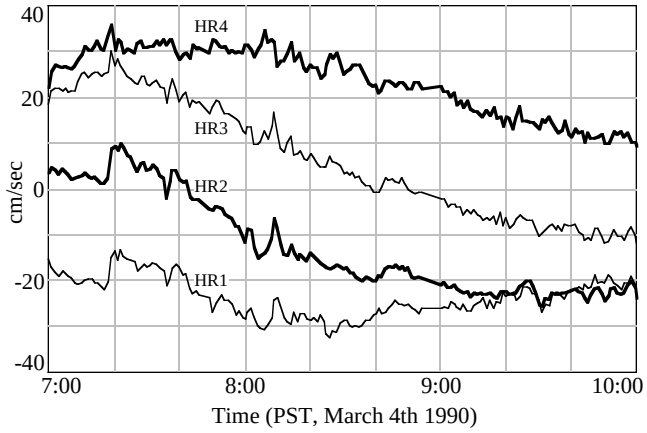

Fig. 6. The along-beam means corresponding to each 1-min average, as shown in Plate 2. A positive velocity corresponds to mean flow away from *FLIP* along the beam. The beams are spaced 45° in azimuth, so that, for example, beams HR2 and HR4 are an orthogonal set.

from periodic satellite fixes, LORAN readings, and accelerometer data.

From about 0730 onward, the stripes along all four beams in Plate 2 are consistent with highly elongated features oriented with major axes roughly perpendicular to beam 2 (as shown in Figure 3), which are simply advected by the mean flow. For example, at 0740 the stripes appear at fixed range on HR2, while they approach *FLIP* on HR1 at about the same rate that they recede on HR3, and they recede more quickly along HR4. The slopes of the stripes in Plate 2 match the measured means flow along each beam (Figure 6), within the accuracy of slope measurements made by holding a ruler over the figure. These observations are consistent with Langmuir circulation oriented with streaks parallel to the dominant wave direction, but not absolutely uniform in that direction (i.e., irregular streaks).

Aliasing of surface wave energy through the time-averaging process is not a significant effect in the data shown in Plate 2. From the estimated wave spectra, wave aliasing could contribute 0.2 to 0.3 $(cm/s)^2$ of variance, compared to observed (cross-wind) noise levels of 1.6 to 2.0 $(cm/s)^2$, and observed signals of 25 to 100 $(cm/s)^2$. Such wave aliasing would affect the downwave beam, HR4, most strongly. Plate 2 does suggest noisier data along HR4. In fact, the noise level is larger than aliasing alone would account for. Wave breaking, which also would tend to line up with HR4, probably contributes to this. In spite of the increased noise level, the features described above remain visible along HR4.

The surface velocity data indicate evolution of the scale of flow during the initial phase of development. The signs of Langmuir circulation are seen most clearly in the cross-wave direction, along beam 2 (HR2). A time series of wavenumber spectra was formed with data from HR2. A range interval from 108 m to 360 m was chosen (85 range bins). The data were detrended, Hamming-windowed, and zero-padded to 128 points before applying an FFT. The resulting contours of the spectral density of velocity variance, plotted against both wavenumber and time, show the evolution in scale of the cross-wave component (along HR2) of the motion at the surface (Plate 3). For reference, a curve corresponding to a linear increase in spacing at a rate of 40 m/h is shown (this is for reference only; it is not an objective fit to the data). The spacing of activity first seen in Plate 2 along HR2 is about 16 m "streak to streak." The wavenumber spectra from HR2 show that weaker activity preceded this at smaller scales (to about 11 m spacing), but the peak appearing at about 0.062 cpm (16 m spacing) is much higher than any preceding peaks in the time series of wavenumber spectra. The ensuing evolution to larger scales is rapid over the next 50 min or so, at which point the dominant scale (in the direction of HR2) is about 50 m streak to streak.

A measure of the dominant scale is provided by a weighted average of the alongbeam wavenumber. To obtain a reasonable estimate, a "noise level" of 12.5 $(cm/s)^2$ per cpm was first subtracted. This corresponds to a total noise level of about 2 $(cm/s)^2$, which is consistent with both the background level seen in Plate 3 and also with noise levels observed elsewhere with this instrument [*Pinkel and Smith*, 1991]. Negative values were then zeroed, and the remaining positive spectral densities were squared. Weighting by the square of the density yields a wavenumber near the location of (single) peaks in power density, but without suffering the "jumpiness" of selecting the maximum discrete estimate. Although somewhat ad hoc, this provides a satisfactory measure of the dominant scale along each beam as a function of time. This technique was applied to data from both HR2 and HR3, and the results combined to estimate a vector wavenumber for the streaks. The combined estimate compensates for variations in *FLIP*'s heading. Beams 2 and 3 were used, on the assumption (borne out in retrospect) that the dominant wavenumber of the observed velocity pattern lies between these two beams (although closer to HR2). It is also desirable that these two beams sense similar components of the velocity field (i.e., 45° apart, rather than 90°). Figure 7 shows the results in terms of the corresponding spacing between convergences versus time. It is seen that the geometric correction has little effect on the estimates versus those from HR2 alone. For reference, a line is shown which corresponds to an increase in spacing at a rate of 40 m/h, starting with 0 m at 0721.

The cross-wind surface velocity variance provides a rough index of the kinetic energy (per unit volume) near the surface of the mixed layer. The cross-wind velocity variance versus time is shown in Figure 8a (mean removed, averaged over 108 to 360 m range and over 1 min). It is interesting to compare this with the wind stress (Figure 8b). The curve marked "12-minute smoothing" corresponds to an exponential smoothing with a 12 min time constant (the time constant is chosen by eye; no special significance is attached). The surface velocity variance and smoothed wind stress show similar time variations. In contrast, the time history of spacing (Figure 7) is much less strongly related to either cross-wind velocity variance or wind stress. It appears that the cross-wind velocity variance at the surface is directly related to the recent time history of the wind stress, regardless of the scale of circulation.

3.3 *Density*

At the onset of the wind, the top 15 m of the ocean were weakly stratified, with a buoyancy frequency of about 1.5 cycles per hour (cph)(see Figure 9). Between 15 and 40 m depth, stratification was negligible (less than 0.5 cph). From 40 to 60 m there was another pycnocline (up to 2 cph), then another unstratified zone continuing to about 85 m depth, below which stratification remained above 1.5 cph.

The time series of density profiles from the CTD system provides an excellent indication of the depth and speed of mixing. Plate 4 shows density data from the top 40 m over the time period of initial growth, from 0700 to 1000 PST, March 4, 1990 (these data were edited and converted to density by S. Anderson;

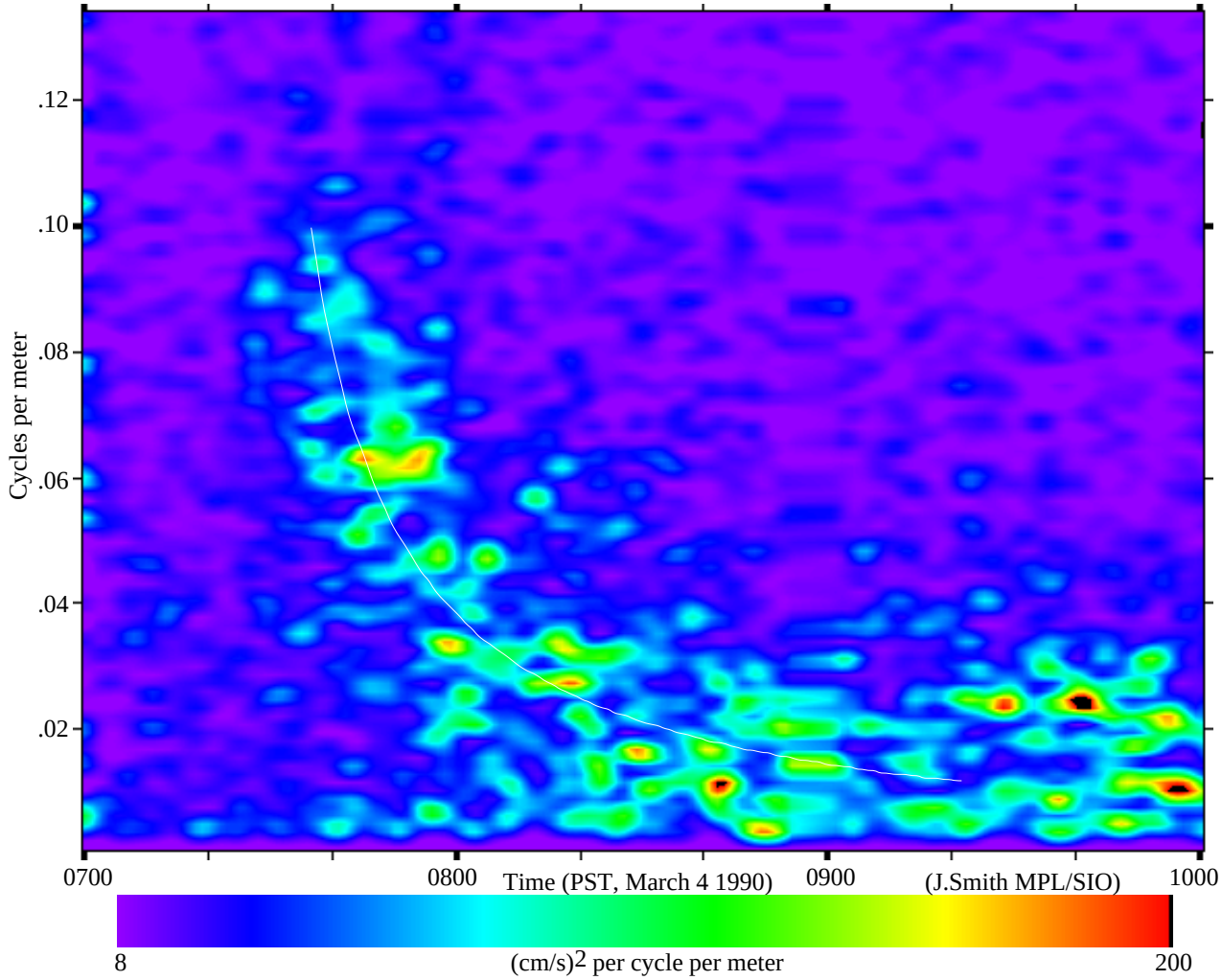

Plate 3. Spatial spectra of cross-wave velocity versus time, from beam 2 (the contour interval is linear). For reference, a curve is superimposed that corresponds to a linear increase in spacing with time, at a rate of 40 m/h (the curve extrapolates to zero spacing at 0721). Note that the velocity variance is confined along a "ridge" roughly centered on this curve. For example, at 0.062 cpm (16 m spacing), the density rises to more than 200 $(cm/s)^2$/cpm at 0745, and then drops nearly to the noise level again by 0810.

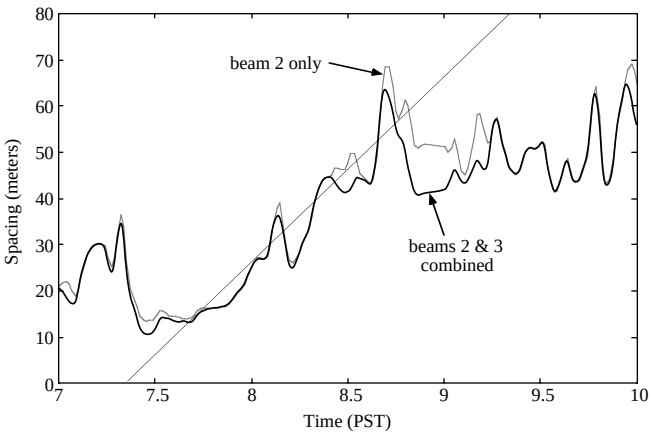

Fig. 7. Weighted mean spacing vs. time, over the same time period as Plates 2 and 3 and Figure 6. A "noise level" of 12.5 $(cm/s)^2$ per cpm was subtracted from the spectra of Plate 3 (beam 2); the densities were then squared and used to determine a weighted wavenumber. The same procedure was applied to data from beam 3, and the results combined to estimate a vector wavenumber. This shows the results in terms of the spacing (inverse magnitude of the wavenumber). For reference, a line corresponding to 40 m/h increase is shown.

unreliable data, above about 6 to 7 m depth, are whited out). A range of only 0.06 σ_T units is contoured. For reference, the white line corresponds to deepening at a rate of 20 m/h, starting with 0 m at 0721. Active mixing is evident in the density profiles after about 0740, when the reference line passes 6 m depth. Note, in particular, the "floating blobs" of denser water in the mixed layer; e.g., at 10-13 m depth at 0820. The existence of these features imply strong mixing; they are not attributable to intrusions, as the plot is of σ_T, not salinity or temperature. To obtain an objective measure of "mixed layer depth" (MLD), a standard technique is employed: the depth is taken where a set increase in density occurs, relative to the shallowest "good" value (6 m is chosen here). The results, along with the reference line, are shown in Figure 10.

To the extent that the "reference lines" fit the data (for both the mixing of density and for the velocity spectra above), the "streak spacing" is just twice the mixed layer depth. The implication is that the horizontal over vertical scale (aspect ratio) of the rolls is 1.0 in this case. In contrast, *Smith et al.* [1987] found an aspect ratio of 1.5 for "quasi-steady" conditions. A plausible explanation is that, during this initial rapid-growth phase, the stratification is less important in determining the form of circulation than in the

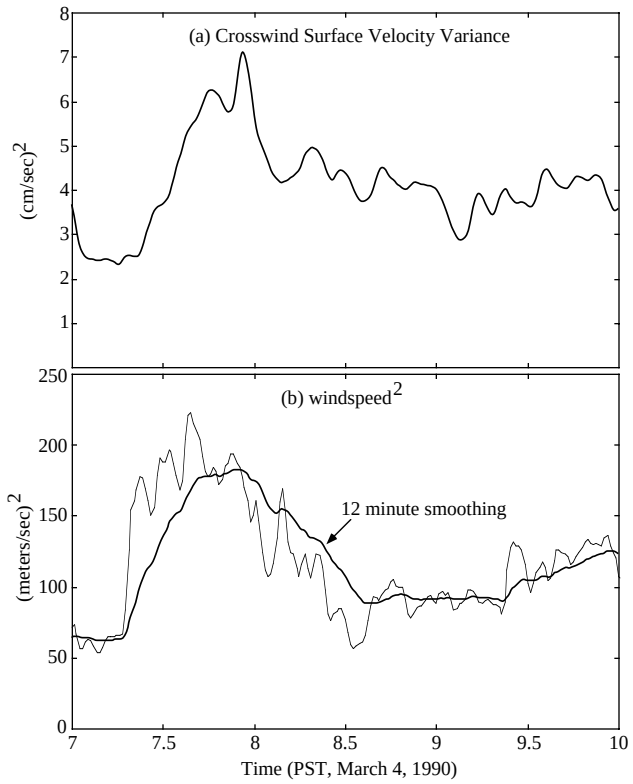

Fig. 8. (*a*) Cross-wind velocity variance versus time (from HR2, means removed). (*b*) For comparison, the wind stress and an exponentially weighted average of the wind stress are also shown (the time constant of 12 min was selected for a good visual fit). The correspondence between (*a*) and (*b*) is reasonably good; the lack of correspondence between (*a*) and Figure 7 demonstrates little influence by the scale of the flow.

case described by Smith et al., in which the circulation was depth-limited by a stronger pycnocline (see also the discussion, below).

3.4 *T-S Characteristics*

During much of the SWAPP experiment, temperature and salinity profiles reflected "intrusive features," attributable to the proximity of a front. This was especially true of the region between about 40 m and 100 m depth. However, over the 3 hours discussed here, and over the top 30 m, temperature dominated the density variations. A *T-S* scatter plot (temperature versus salinity) is shown for data taken between 0730 and 0900 PST, and between 7 m and 27 m depth (Figure 11). This covers the time-space section of the most active mixing. The *T-S* plot is dispersed slightly along *S* because of (1) salinity spiking (which arises from the differing time constants of the temperature and conductivity sensors), (2) the salinity variations being close to the resolution limit of the instrument, and possibly (3) effects due to bubbles in the mixed layer. The *T-S* plot is roughly consistent with simple mixing throughout the time-depth section (the points lie along a line, with some scatter). It also demonstrates clearly that salinity was of secondary importance in determining density variations throughout this time-space section. In fact, on the basis of the *T-S* diagram, one might argue in favor of using just temperature data for analysis, since the salinity is approximately constant, and the conductivity measurement is more prone to disturbance by bubbles and flushing characteristics. Density plots were used above, since they have more direct appeal; however, the corresponding temperature plots are nearly identical.

Is it possible to explain the evolution of the density field in terms of advection, or an intrusion? Several aspects of the observed *T-S* field argue against this possibility. First, such intrusions usually have markedly different *T-S* characteristics, typically with water from the two sides of a front lying along different lines which overlap in density. This *T-S* plot (Figure 11) shows no such pattern. As mentioned above, the density field is described well by just temperature, between the hours of 0700 and 1000, and from 6 to 30 m depth. The temperature at 7 m depth reflects the density of the developing homogeneous layer (after about 0730), while the average from 7 to 30 m reflects the total heat content of the layer. As seen in Figure 12, the heat content is nearly constant (with small variations attributable to internal wave activity), while the temperature of the well mixed layer steadily decreases. This is consistent with local mixing in the vertical, but would be extremely unusual for an intrusion. Second, the homogeneous layer changes density with time, as can be seen in the density plot (Plate 4). For an advected feature in quasi-geostrophic balance, the implied vertical isopycnals would require vertical shears in the horizontal flow. This would be unstable because of the low stratification in the layer. Finally, the observed existence of blobs of denser and lighter water, suspended within the mixed layer, are amenable to only a dynamic explanation (these appear also plots of temperature alone and so are not artifacts of salinity spiking or bubble clouds). These are observed to be transient phenomena and are clearly not in static equilibrium; rather, they indicate active mixing. Each of these points alone is strong evidence for mixing over advection; taken together, they rule out a purely advective explanation.

4. DISCUSSION

What parameters are relevant to the development of such a mixed layer? In the 2 or 3 hours of initial development described here, it is reasonable to discount rotational effects; i.e., instabilities of the Ekman layer [c.f. *Leibovich and Lele,* 1985]. For this time period, a reasonable theory for generation of

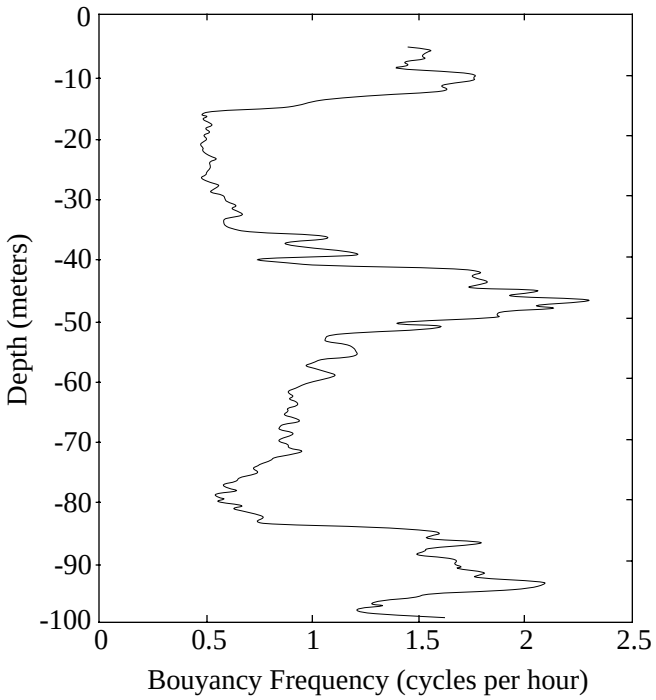

Fig. 9. Profile of buoyancy frequency, averaged over the hour prior to the wind jump. Note the stratification over the top 15 m, from 40 to 50 m, and below 85 m.

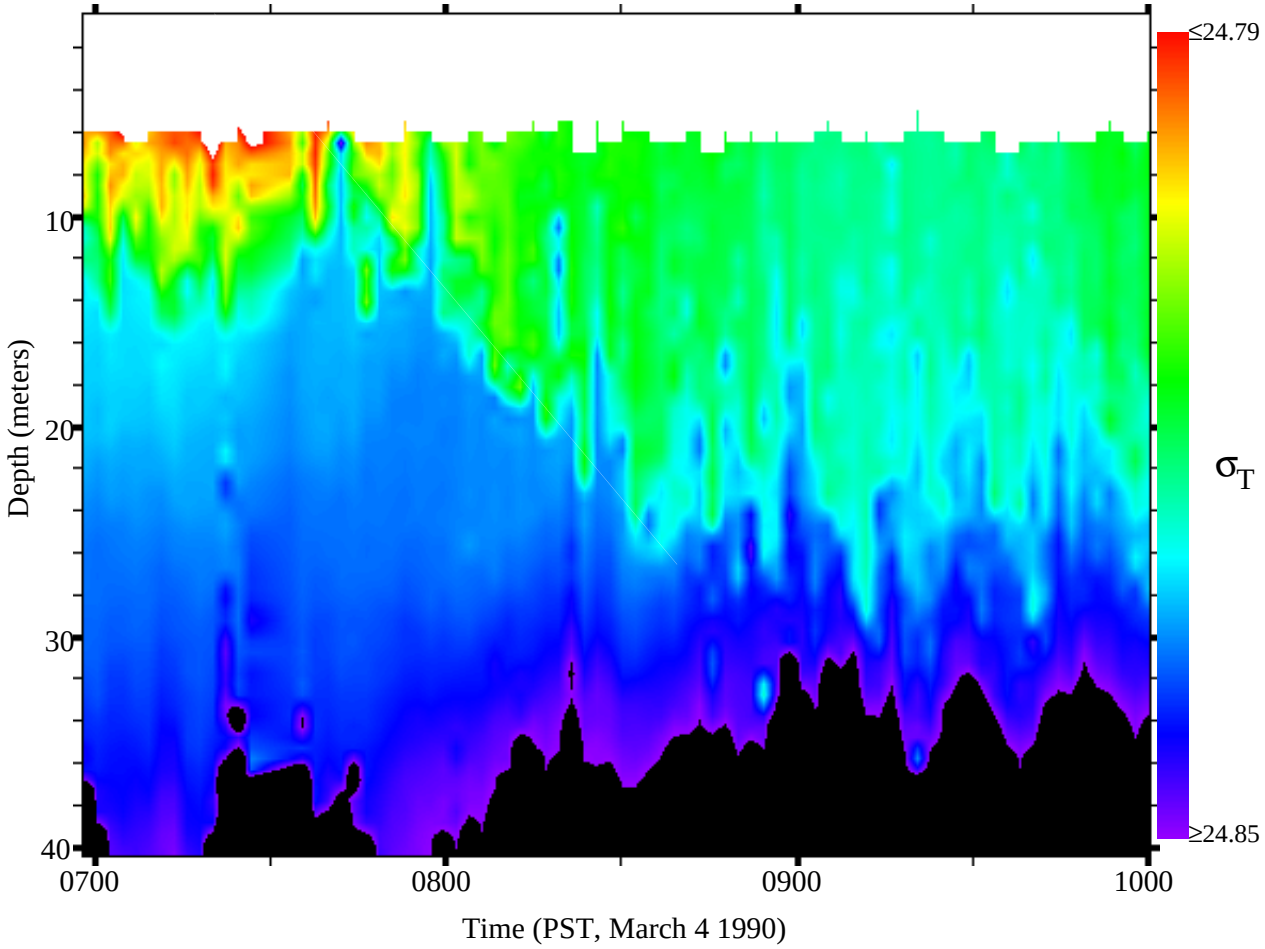

Plate 4. Density profiles over the same time period, 0700-1000 PST, March 4. A narrow range of densities contoured: from 24.78 to 24.855 kg/m^3. The contour interval is 0.005 σ_T units, kg/m^3. The superimposed straight line corresponds to a depth increase at a rate of 20 m/h, beginning with 0 m at 0721. Note the "blobs" of denser water appearing within the mixed layer; e.g, at 0820 between 10 and 16 m depth, and at 0850 near 17 m depth. There also appear to be blobs of lighter water below the thermocline, for example just before 0900 at 33 m depth.

Langmuir circulation is that which has come to be called "CL2," denoting the second version of a theory based on equations derived by *Craik and Leibovich* [1976] (see also *Garrett* [1976], and *Leibovich* [1983]). In the following, the observations are discussed in the context of this wave-current interaction mechanism. It is also possible to compare the mixing with that due to shear-generated turbulence, without appeal to wave effects. For example, comparisons could be made with recent laboratory

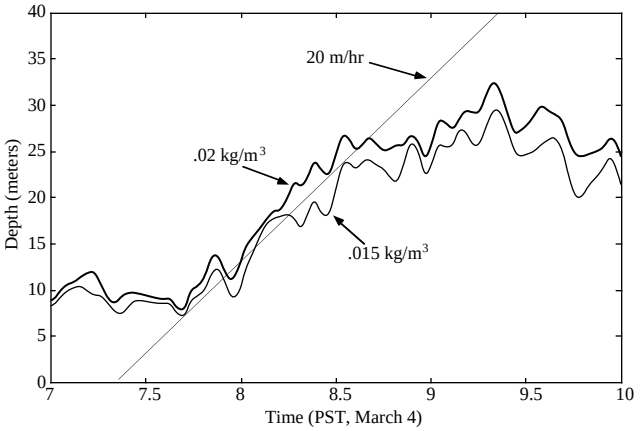

Fig. 10. Mixed layer depth versus time. This is estimated from a set increase in density over the value at 6 m (the shallowest dependable data point). The results using two increments are shown: 0.02 and 0.015 σ_T units. Also shown is a reference line, 20 m/h. From 0740 to 0830 the two incremental results roughly span the reference line.

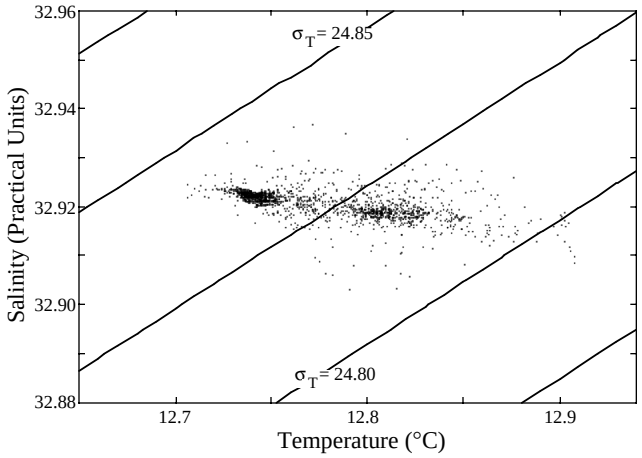

Figure 11. Scatter plot of *T* (temperature, degrees Celsius) vs. *S* (salinity, practical salinity units). All data points between 0730 and 0900 and between 7 m depth and 27 m depth are shown, inclusive. Salinity is of minor importance compared to temperature for this section, which covers the most active mixing.

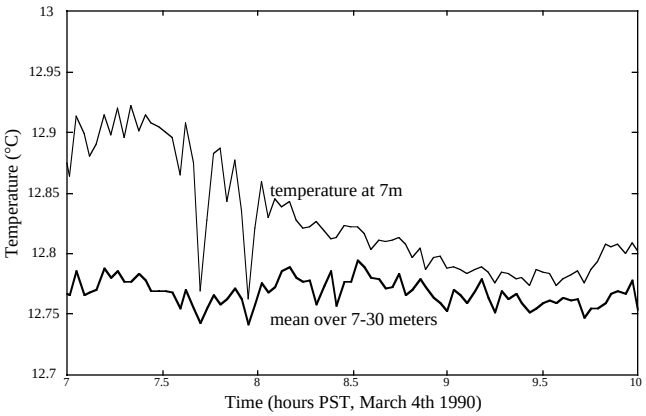

Figure 12. Temperature at 7 m depth (representative of the homogeneous layer), and the average temperature over 7 to 30 m depth (representative of the heat content in the top 30 m of the ocean), versus time. The heat content is essentially constant, with variations attributable to internal waves. The temperature of the homogeneous layer steadily decreases as the layer deepens.

work, in which surface waves are absent [e.g., *Rohr and Van Atta,* 1987]. The CL2 theory is appealing for the relative ease with which the relevant parameters can be estimated. Further work, both theoretical and observational, will be required to distinguish whether the wave effects are significant or not.

4.1 *Definition of Parameters*

In the CL2 theory, the circulation arises as an instability of the wind-driven flow under the influence of surface waves. The waves enter via induced Lagrangian drift (Stokes' drift). For a single wave component, the Stokes' drift can be written as

$$\mathbf{U}^S(z) = \langle \int \mathbf{u}^w dt \cdot \nabla \mathbf{u}^w \rangle = ka^2\sigma\, e^{-2kz} \tag{1}$$

where a, σ, $\mathbf{k}$, and $\mathbf{u}^w$ are the amplitude, frequency, (vector) wavenumber, and (vector) orbital velocity of the surface wave, respectively; also, $k \equiv |\mathbf{k}|$, and angle brackets denote an average over wave phase. Since this varies with depth, it distorts the vorticity of the mean flow and of the growing instabilities. The sense of this distortion is such that surface water is induced to flow toward maxima in the downwind surface current perturbations. As fluid flows along the surface toward these maxima, it is also accelerated downwind by the wind stress. The net effect is that patterns resembling Langmuir circulation are reinforced.

Three parameters arise from scaling the governing equations [*Leibovich,* 1983]. One is the "Langmuir number,"

$$La \equiv \frac{k^2\nu_T}{(U_z^S U_z)^{1/2}} = \left(\frac{k^2\nu_T^3}{2\sigma a^2 u_*^2}\right)^{1/2} \tag{2}$$

where ν_T is the kinematic "eddy" viscosity, U_z^S is the Lagrangian shear ($\partial U^S/\partial z$), U_z is the mean shear (in general these are functions of depth), and u_* is the friction velocity in the water. This represents the balance between forcing, $(U_z^S U_z)^{1/2}$, and viscous damping, $k^2\nu_T$. The second is a "Richardson number," balancing the forcing against stratification:

$$Ri \equiv \frac{N^2}{U_z^S U_z} \tag{3}$$

where N^2 is the buoyancy frequency. The third parameter is the (turbulent) Prandtl number, the ratio of diffusivities of density versus momentum; its importance here has not been explored (to the author's knowledge). The two principle parameters *La* and *Ri* may be recast into other forms, with other scaling choices [c.f. *Leibovich et al.*, 1989].

4.2 *Evaluation of Parameters*

The Lagrangian shear $U_z^S(z)$ may be estimated from the sonar measurements. First, equation (1) can be manipulated to yield a spectral density of $U_z^S(z)$ in terms of the surface wave slope spectral densities:

$$\begin{aligned}\hat{U}_z^S(z,\sigma) &= a^2(\sigma)\, 2k_x k\sigma\, e^{-2k} \\ &= 2\sigma\,(S_{xx}(S_{xx}+S_{yy}))^{1/2}\, e^{-(2z/g)\sigma^2}\end{aligned} \tag{4}$$

where $S_{xx}(\sigma)$ is the downwind slope spectral density, and $S_{yy}(\sigma)$ is the cross-wind slope density. The slope spectra can be converted from velocity component spectra. For example, given a spectrum of the x component of surface orbital velocity, $\hat{V}_x^2(f)$, formed from the Doppler sonar measurements, $\sigma S_{xx}(\sigma) = (2\pi/g)^2\, f^3\, \hat{V}_x^2(f)$ (Figure 13). As seen in Figure 13, the spectrum of contributions to $U_z^S(z)$ is nearly flat at the higher frequencies.

An approximate wave spectrum provides results with negligible error, and which are more easily generalized. From wave spectra

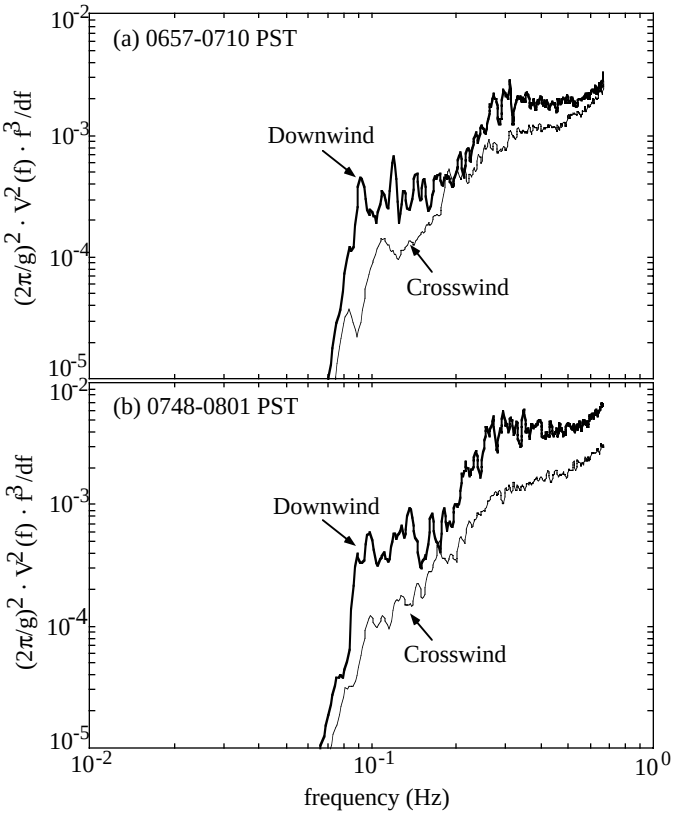

Fig. 13. Equivalent frequency-weighted slope spectra, from the HR sonar data, for (*a*) just before and (*b*) just after the increase in wind. A slope spectrum of the form $S_{xx}(\sigma) \approx B\sigma^{-1}$ would appear flat in this figure. For modelling purposes, the S_{xx} (downwind) spectra are broken into two flat segments, from f=0.088 Hz to 0.26 Hz, and from 0.26 Hz up. The lower frequency segment is fit with B_1=0.0003 (before) and 0.00045 (after); the upper segment is fit with B_2=0.002 (before) and 0.0045 (after). The cross-wind component S_{yy} appears to be about half the magnitude of the downwind component.

just before the onset of the Langmuir circulation (Figure 13a), it appears reasonable to take $S_{xx}+S_{yy} \approx 1.5\, S_{xx}$, and let $S_{xx}(\sigma) \approx B\sigma^{-1}$ with B non-zero and constant over two segments: $B_1 \approx 0.0003$ from $f_1 \approx 0.088Hz$ to $f_2 \approx 0.26Hz$, and $B_2 \approx .002$ from f_2 up to some high-frequency cutoff f_c. The spectra afterwards (Figure 13b) yield $B_1 \approx 0.00045$ and $B_2 \approx 0.0045$, with the other parameters unchanged. Neglecting capillarity, this leads to

$$U_z^S(z) = 6^{1/2}\left(B_1 \int_{\sigma_1}^{\sigma_2} e^{-(2z/g)\sigma^2}\, d\sigma + B_2 \int_{\sigma_2}^{\sigma_c} e^{-(2z/g)\sigma^2}\, d\sigma \right)$$

$$= \left(\frac{3\pi g}{4z}\right)^{1/2}\left[B_2 - (B_2-B_1)\mathrm{erf}\left((2k_2 z)^{1/2}\right) - B_1 \mathrm{erf}\left((2k_1 z)^{1/2}\right)\right] \quad (5)$$

where $2\pi\sigma_n \equiv f_n$ and $k_n \equiv \sigma_n^2/g$. The high-frequency cutoff σ_c is assumed to be large: for σ_c near the gravity-capillary transition, the above is valid for depths greater than a millimeter or two. Near the surface, where $2k_2 z \ll 1$, (5) is given approximately by

$$U_z^S(z) \approx 6^{1/2}\left\{ B_2\left(\frac{\pi g}{8z}\right)^{1/2} - (B_2-B_1)\sigma_2 - B_1\sigma_1 \right\} \quad (6)$$

Figure 14 illustrates equations (5) and (6) for the conditions just before and after the observed growth of Langmuir circulation. Also shown is a curve corresponding to (5), but neglecting the lower frequency segment (from 0.088 to 0.26 Hz). This figure illustrates several things: (*i*) The approximation (equation 6) always underestimates the Lagrangian shear; it is reasonable for depths less than a meter, or $(4k)^{-1}$ referred to the 4-s peak waves.

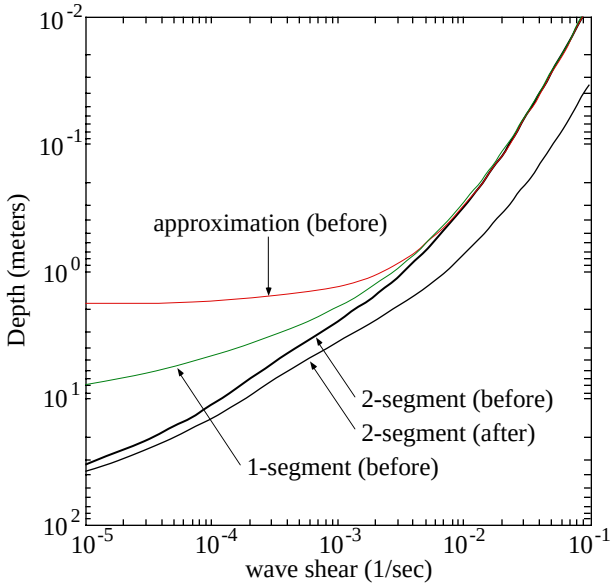

Fig. 14. Lagrangian shear $U_z^S(z)$ due to the presence of the irrotational waves. These are computed from spectra based on Figure 13. The two-segment spectra provide accurate models of the measured spectra. Also shown is the shear resulting from just the higher frequency (steeper) segment, and an approximation valid just near the surface (equation (6); see text for details). Note that the two-segment curves (before and after the change in wind) have two "break points" in depth, one at about 2 m, and the other at about 20 m. The former corresponds to $(2k)^{-1}$ for 4-s waves, the latter for 10-s waves. Above the break point, the location of the low-frequency wave cutoff (peak) has little influence on the shape of the shear profile. Near the surface (where the approximate solution is accurate), the profile is roughly proportional to $z^{-1/2}$.

(*ii*) The single-segment version of equation (5) also departs from the two-segment version below a meter depth, but more slowly than equation (6). (*iii*) The shear in the top meter increases in direct proportion to the spectral level B_2 (as is to be expected). (*iv*) Finally, the near-surface profile is independent of the peak frequency: the peak frequency only sets a boundary below which the shear essentially vanishes.

The shear at the actual surface is

$$U_z^S(z) = 6^{1/2}\left[B_2\sigma_c - (B_2-B_1)\sigma_2 - B_1\sigma_1\right] \approx 6^{1/2}\, B_2\sigma_c \quad (7)$$

The effect of a finite high-frequency cutoff can be emulated by adding z_o to z, where $z_o = \pi g/8\sigma_c^2 = \lambda_c/16$. For example, at the gravity-capillary transition, $\lambda_c \approx 1.7$ cm, for which $z_o \approx 1$ mm.

Realistic profiles of $U_z^S(z)$, as exemplified by (5), have considerably more curvature near the surface than an exponential profile based on the "dominant" waves. There is no subrange of depth in which a linear profile is appropriate: at small depths, the profile of Lagrangian shear is roughly proportional to $z^{-1/2}$. Nor is there a depth below which the profile becomes nearly exponential: as depth increases, the bandwidth of waves reaching that depth decreases rapidly, leading to superexponential decay.

It is somewhat more difficult to estimate (or measure!) the Eulerian mean shear in the top meter or two of the ocean. However, to this end, consider the turbulent flow near the surface before it is modified by the developing Langmuir circulation. Observations suggest that below a wave amplitude or so, the mean shear and turbulence scale roughly according to the "inner law" for wall-bounded turbulent flow [e.g., *Jones*, 1985]. Within a few wave amplitudes of the surface, wave breaking may inject energy directly into the turbulence, and this could alter the turbulent profile. For example, if the effects of breaking waves resemble those of dragging isolated objects along the surface, one could apply arguments appropriate to turbulent wakes [e.g., *Tennekes and Lumley*, 1972, pp. 113-124]. Such wakes can have the proper form to trigger a Langmuir circulation instability: they have downwind maxima at the surface and can be elongated in the alongwind direction. Pursuit of such a model is beyond the scope of this paper.

It is instructive to examine the results of the assumption that inner-law scaling remains approximately correct. According to the "law of the wall,"

$$U_z \approx u_*/\kappa z \quad (8)$$

and $\nu_T \approx \kappa z u_*$, where κ is von Karman's constant (≈ 0.4). Also, $\alpha_T \propto \nu_T$ (where α_T is the diffusivity of density). Using these values for ν_T and U_z, and using U_z^S from equation (5), $La(z)$ may be estimated. Using a constant buoyancy frequency of 1.5 cph (based on Figure 9), $Ri(z)$ can also be estimated. These are shown in Figure 15; note La and Ri are scaled by their critical values, 1/3.04 and 1/4, respectively.

Figure 15 illustrates three things: (1) The profiles are strongly depth dependent. For small depths, $La \propto z^{7/4}$, and (for constant N^2) $Ri \propto z^{3/2}$. (2) La does not change much before and after the wind increases (using steady state values of ν_T and U_z). The transition from supercritical to subcritical values of La occurs near 3 m depth (i.e., viscous damping is significant relative to direct forcing below 3 m). (3) Although Ri does change, it is always much farther than La from its critical value (i.e., stratification ought to be unimportant initially). The transition $Ri \approx 1/4$ occurs at 7 m depth before, and 10 m depth after the wind increases. Using $Ri \approx 1/8$ (based on the comments of *Leibovich* [1983]), the transitions occur at about 5.5 m and 8 m, still twice as deep as the

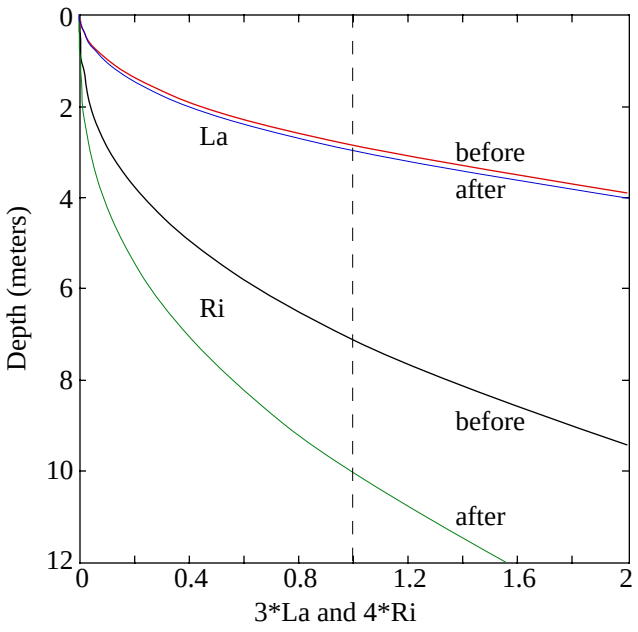

Fig. 15. Profiles of $La(z)$ and $Ri(z)$ before and after the sudden change in wind. "Inner scaling" is used, as for wall-bounded turbulent shear: $\nu_T \approx \kappa z u*$ and $U_z \approx u*/\kappa z$. These are scaled by their critical values, 1/3.04 and 1/4 respectively; stability is implied to the right of the dotted line. Note that (1) La is supercritical only above about 3 m depth, and changes little before and after the wind changes; and (2) Ri is farther from its critical value than La: stability from Ri is implied below about 6 or 7 meters (before), or 8 to 10 meters (after). In other words, the equations are viscously damped below 3 m, while stratification is a significant stabilizing influence only below 6 to 10 m.

"critical depth" for La. Another argument against the dynamic importance of stratification in the initial development lies in the obeserved aspect ratio: if stratification is important (as, for example, in the case discussed by *Smith et al.* [1987]), the aspect ratio should be greater than 1; i.e., the circulation should tend to be shallower than it is wide.

The above considerations leave a puzzle: if La is the controlling parameter, and it does not change significantly before versus after 0721 PST, why is no circulation observed before then? The wind blew at 8 m/s for over an hour prior to 0721 (see Figure 2). This is usually sufficient wind and time for Langmuir circulation to form.

4.3 *Comparison With Previous Calculations*

To be realistic, the depth dependence of the parameters ν_T, Ri, La, and Pr should be taken into account. However, theoretical developments to date have assumed constant eddy viscosity, most assume constant mean shear, and many assume constant values of Ri and La.

The computations most nearly relevant to the present comparison appear to be those of *Leibovich and Paolucci* [1981] (hereinafter "LP"). These include vertical variation of the Stokes drift of the form given by (1), and allow the mean flow to develop with the onset of wind. However, ν_T is taken as constant, the waves do not evolve, and only a single "peak" wave component is considered. Also, the results concern mainly the asymptotic behavior ($t \rightarrow \infty$) of the evolving flow. Consequently, these may be interpreted in terms of the asymptotic form of the currents; in particular, the mean shear becomes constant. According to *Leibovich* [1983], only the calculations for negligible stratification were accurate. Subsequent recalculations [*Leibovich*, 1983] reportedly show significant influences on the form of circulation for $Ri > 1/8$, and stability for $Ri > 1/4$. An earlier analysis [*Leibovich*, 1977] includes depth variations in stratification (N^2); however, viscosity is neglected. The most unstable mode in this case has infinitesimal horizontal and vertical scale. In the present case, viscosity appears to be more restrictive than stratification (Figure 15), and so LP appears more appropriate. Some recent calculations [*Leibovich et al.*, 1989] explore a range of both La and Ri (particularly near neutral stability). These reveal interesting behavior in the nonlinear evolution of Langmuir-like circulation. However, both the mean flow and Stokes drift are assigned linear profiles (constant shears), and so (again) comparison is less apt.

A major difficulty in comparing the present data with LP lies in evaluation of La. In LP, La varies with depth due to only the exponential form for U_z^S; ν_T and (effectively) U_z are assumed constant. (The values of La referred to in LP are surface values.) This exponential form is incompatible with the form suggested above, which is proportional to $z^{7/4}$ at small depths. Still, perhaps a "bulk estimate" La_b is possible. The absence of observed Langmuir circulation before 0720 suggests that a bulk estimate La_b was larger than the critical value before 0720, and less afterward. How can this be resolved with Figure 15, which shows little change in La?

Perhaps La_c is between the before and after values of La_b. For marginally unstable conditions, LP find the most unstable mode at non-dimensional wavenumber $k* \approx 0.32$ (see Figure 16, based on a figure from LP). Length is scaled by k, the wavenumber of the dominant surface waves, so the marginally unstable mode has a cross-wind wavelength about 3 times the dominant surface wavelength. When Langmuir circulation is first seen in the data presented here (around 0730 PST), the dominant-slope waves had about a 4 s period, or 25 m wavelength. Thus at marginal stability, the preferred scale would be about 80 m between

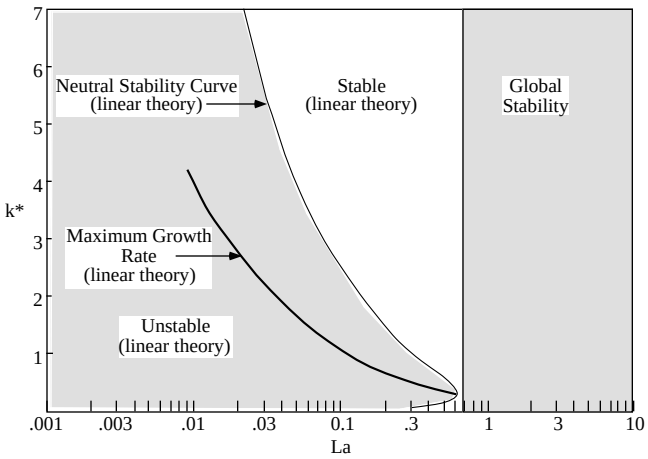

Fig. 16. Stability diagram for Langmuir circulation with negligible stratification (based on *Leibovich and Paolucci* [1981]). The region marked "global stability" is derived from an energy analysis (see *Leibovich and Paolucci* [1981] for details). Of interest are the curves from the linear theory of initial growth, and particularly the curve of maximum growth rate versus La and $k*$. The definition of La used by Leibovich and Paolucci differs from that used here by a factor of 2, so this whole graph should be shifted; for example, their critical value of 1/1.52=0.66 should be translated to $La_c \approx 0.33$. The initial scale observed here corresponds to $k* \approx 1.6$, which would correspond to $La \approx 0.09\ La_c$.

streaks. This is significantly larger than the observed initial scale of 11 to 16 m.

Alternatively, perhaps the waves, mean shear, and subsurface turbulence (hence ν_T) evolve at different rates after a change in stress. The greatest change in La allowed by (3) would occur if both U_z and U_z^S adjust quickly, while ν_T lags behind. Leaving aside the question of whether this is reasonable, this would make $La \sim U_{10}^{-2}$ on a short time scale, and so $La \geq (8/13)^2 La_C \approx 0.4 La_c$ just after the increase in wind. From Figure 16, this yields $k^* \approx 1/2$, or about 50 m spacing between initial streaks. This is still rather large. For reference, the observed initial scale of ≤16 m would correspond to $k^* \geq 1.6$, or $La \leq 0.09\ La_c$.

There are two more considerations: (1) A longer period swell (about 11 s) also preceded the wind, with less slope variance, but more velocity variance (these differ in proportion to f^2) than the 4-s "seas"; thus the appropriate wave scale is arguably larger than taken above. (2) The effective depth of the sonar measurements is about 1 to 1.5 m; motion with smaller vertical scales is filtered out. The spatial spectra shown in Plate 3 show activity down to about 11 m spacing, preceding the big peak at 16 m spacing. Even smaller scales may have preceded this, yet gone undetected owing to smaller vertical extent. Both considerations suggest an even greater discrepancy between the observed and modelled initial scales. Thus it seems fruitless to pursue the comparison further. Apparently, the forcing contains smaller scales than assumed in LP.

4.4 *Speculation*

There are several possible explanations for the observed sequence of events. (1) Stability could have been controlled by variations in the shear at the base of the mixed layer, due to the internal wave field. Near-inertial shears were fairly strong over this period [R. A. Weller, personal communication, 1991]. (2) Langmuir circulation could have been present before 0720, but not yet large enough (deep enough) to be observed, and growing only slowly. This is compatible with Figure 15, which implies arbitrarily small initial growth scales, and provides no basis for excluding development before 0720. (3) A change in buoyancy flux at the surface could contribute to the differences before and after 0720. However, Figure 12 indicates no discernable change in heat content, and Figure 11 implies no discernable change in salt content over the period of rapid mixing. (4) Perhaps the stratification in the uppermost 5 m (out of range of the CTD measurements) was much stronger than that from 5 to 15 m depth (where $N \approx 1.5$ cph). From Figure 15, N^2 would have to be about 12 times larger than estimated in order to make Ri (before) comparable to La at 3 m depth, where $La \approx La_c$; yet the heat content in the layer above must not be large enough to influence the heat budget. This seems rather unlikely. (5) It is possible that the different components of La have unexpectedly large transient responses, allowing the instability to get started upon a sudden increase in wind. Presumably, the stability and development of finite-amplitude circulation could obey different bounds, or (in other words) the circulation could significantly alter the characteristics of the turbulence which determine ν_T and U_z.

5. CONCLUSIONS

The data described here present a straightforward picture of energetic "roll vortices," with rapid mixing into a weakly stratified surface layer. Within minutes after a sudden increase in wind, the roll vortices are observed to grow rapidly in spacing and depth. The picture presents a dual challenge: to explain the absence of observed Langmuir circulation before the increase in wind, and to explain the initial scale and simple evolution afterward. Specifically, several features are worthy of note:

(1) During the rapid growth phase observed here, the "cells" of the circulation have an aspect ratio of about 1.0. This contrasts with a ratio of 1.5 previously reported for a case where the circulation was depth-limited by a strong pycnocline [*Smith et al.*, 1987]. The isotropic aspect ratio argues against the dynamic importance of preexisting stratification in determining the flow in this case.

(2) There is a true temporal cascade to larger-scale circulation. Energy at once dominant scales vanishes as the flow evolves to larger scales. The mean square surface velocity in the cross-wind direction remains roughly proportional to the time-averaged wind stress (e.g., with a 12 min exponential averaging), even as the scale increases.

(3) Models based on the CL2 equations with constant values of U_z and ν_T are inadequate to address the real-world evolution of Langmuir circulation. The depth dependence of La and Ri (and also Pr) must be taken fully into account: (*i*) Based on observed wave spectra, the Lagrangian shear U_z^S depends roughly on $z^{-1/2}$ in the top meter, and is more or less independent of the peak frequency of the waves. This invariance of the upper-most part of the shear profile may help to explain the absence of evidence for the dependence of mixing on wave parameters. (*ii*) "Law of the wall" inner scaling is probably more appropriate to the initial development phase discussed here than (for example) a mean profile based on constant eddy viscosity. This yields $U_z \propto z^{-1}$. (*iii*) With these scalings, and for small depths, $La \propto z^{7/4}$, and $Ri \propto z^{3/2}$. (*iv*) The first scale observed is smaller than can be reasonably extracted from the model of *Leibovich and Paolucci* [1981]. The forcing is implied to contain smaller scales than assumed in the theory (e.g., as portrayed in the preceding point).

The initial growth and development discussed here is new and exciting, but is only part of the whole story. Of equal interest and consequence is the subsequent evolution of the mixed layer, over the duration of the wind event (and the other wind events). The breadth of observations obtained during SWAPP provides an exciting opportunity to advance our understanding of this sequence of events.

Acknowledgments. The author would like to thank R. A. Weller, A. Plueddemann, D. Farmer, R. Pinkel, S. Anderson, and many others for useful conversations concerning this work. Thanks are also due to the many people involved in the collection and analysis of the data. This research is supported by the Office of Naval Research, physical oceanography program, under contracts N00014-89-J-1154 and N00014-90-J-1285.

REFERENCES

Craik, A. D. D., and S. Leibovich, A rational model for Langmuir circulations, *J. Fluid Mech., 73*, 401-426, 1976.

Crawford, C.B., and D.M. Farmer, 1987. On the spatial distribution of ocean bubbles, *J. Geophys. Res., 92*, 8231- 8243.

Garrett, C. J. R., Generation of Langmuir Circulations by surface waves - A feedback mechanism, *J. Mar. Res., 34*, 117-130, 1976.

Jones, I., Turbulence below wind waves, in *The Ocean Surface*, edited by Y. Toba and H.Mitsuyasu, pp. 437-442, D. Reidel, Norwell, Mass., 1985.

Langmuir, I., Surface motion of water induced by wind, *Science, 87*, 119-123, 1938.

Leibovich, S., Convective instability of stably stratified water in the ocean, *J. Fluid Mech., 82*, 561-581, 1977.

Leibovich, S., The form and dynamics of Langmuir circulations, *Annu. Rev. Fluid Mech., 15*, 391-427, 1983.

Leibovich, S., and S.K. Lele, The influence of the horizontal component of Earth's angular velocity on the instability of the Ekman layer, *J. Fluid Mech., 150*, 41-87, 1985.

Leibovich, S., and S. Paolucci, The instability of the ocean to Langmuir circulations, *J. Fluid Mech., 102*, 141-167, 1981.

Leibovich, S., S.K. Lele, and I.M. Moroz, Nonlinear dynamics in Langmuir circulations and in thermosolutal convection, *J. Fluid Mech., 198*, 471-511, 1989.

Pinkel, R., On the use of Doppler sonar for internal wave measurements, *Deep Sea Res., 28A*, 269-289, 1981.

Pinkel, R., and J. Smith, Repeat sequence codes for improved performance of Doppler sounders, *J. Atmos. Oceanic Technol.*, 9, 149-163, 1992.

Pollard, R., and K.J.H. Thomas, Vertical circulation revealed by diurnal heating of the upper ocean in late winter, part 1: Observations, *J. Phys. Oceanogr., 19*, 269-278, 1989.

Rohr, J. and C. Van Atta, Mixing efficiency in stably stratified growing turbulence, *J. Geophys. Res., 92*, 5481-5488, 1987.

Rummler, W.D., Introduction of a new estimator for velocity spectral parameters. *Rep. MM-68-4141-5*, AT&T Bell Labs., Murray Hill, N.J., 1968.

Smith, J.A., Doppler sonar and surface waves: Range and resolution, *J. Atmos. and Oceanic Tech., 6*, 680-696, 1989.

Smith, J.A., R. Pinkel, and R.A. Weller, Velocity fields in the mixed layer during MILDEX, *J. Phys. Oceanogr., 17*, 425-439, 1987.

Thorpe, S., Bubble clouds: A review of their detection by sonar, of related models, and of how K_V may be determined, in *Oceanic Whitecaps*, pp. 57-68, D. Reidel, Norwell, Mass., 1986.

Tennekes, H., and J.L. Lumley, *A First Course in Turbulence*, 300 pp., MIT Press, Cambridge, Mass., 1972.

Weller, R.A., J.P. Dean, J. Marra, J. Price, E.A. Francis, and D.C. Boardman, Three-dimensional flow in the upper ocean, *Science, 227*, 1552-1556, 1985.

Weller, R.A., M.A. Donelan, M.G. Briscoe, and N.E. Huang, Riding the crest: A tale of two wave experiments, *Bull. Am. Meteorol. Soc., 72*, 163-183, 1991.

J. Smith, Scripps Institution of Oceanography, University of California at San Diego, La Jolla, CA 92093-0213.

(Received September 20, 1991;
revised December 16, 1991;
accepted December 16, 1991)